Article

The Effect of Different Configurations of Copper Structures on the Melting Flow in a Latent Heat Thermal Energy Semi-Cylindrical Unit

Mohamed Boujelbene [1] , Amira M. Hussin [2], Seyed Abdollah Mansouri Mehryan [3,*] and Mohsen Sharifpur [4,5,*]

1   Industrial Engineering Department, College of Engineering, University of Ha'il, Ha'il 55476, Saudi Arabia; mboujelbene@yahoo.fr
2   Department of Mathematics, Al-Aflaj College of Science and Humanities, Prince Sattam bin Abdulaziz University, Al-Aflaj 710-11912, Saudi Arabia; a.hussin@psau.edu.sa
3   Young Researchers and Elite Club, Yasooj Branch, Islamic Azad University, Yasooj 1987, Iran
4   Department of Mechanical and Aeronautical Engineering, University of Pretoria, Pretoria 0002, South Africa
5   Department of Medical Research, China Medical University Hospital, China Medical University, Taichung 404, Taiwan
*   Correspondence: s_mansourimehryan@sbu.ac.ir or alal171366244@gmail.com (S.A.M.M.); mohsen.sharifpur@up.ac.za (M.S.)

Abstract: Utilizing latent heat thermal energy storage (LHTES) units shows promise as a potential solution for bridging the gap between energy supply and demand. While an LHTES unit benefits from the latent heat of the high-capacity phase change material (PCM) and experiences only minor temperature variations, the low thermal conductivity of PCMs hinders the rapid adoption of LHTES units by the market. In this regard, the current work aims to investigate the thermal behavior of a semi-cylindrical LHTES unit with various copper fin configurations (including horizontal, inclined, and vertical fins) on the melting flow. The novelty of this research lies in the fact that no prior studies have delved into the impact of various fin structures on the thermal performance of a semi-cylindrical LHTES system. The nano-enhanced phase change material (NePCM) fills the void within the unit. The warm water enters the semicircular channel and transfers a portion of its thermal energy to the solid NePCM through the copper separators. It is found that the system experiences the highest charging capability when the fins are mounted horizontally and close to the adiabatic upper wall. Moreover, the presence of dispersed graphite nanoplatelets (GNPs) inside the pure PCM increases the charging power and temperature of the LHTES unit.

Keywords: copper fin; enthalpy–porosity technique; graphite nanoplatelet; latent heat thermal energy storage unit; melting flow; nano-enhanced phase change material; semi-cylindrical unit

MSC: 76R10; 80A22; 80M10

1. Introduction

Phase change materials (PCMs) have garnered significant attention for various applications due to their exceptional capability to store substantial thermal energy. PCMs find applications in diverse areas, such as battery cooling [1], solar power systems [2,3], heating and cooling of buildings [4,5], cooling of electronic equipment [6], and food drying [7]. These applications leverage the unique thermal energy storage properties of PCMs to enhance performance and efficiency in various industries. Despite the numerous advantages of latent heat thermal energy storage (LHTES) systems, it is important to note that many commercially available PCMs suffer from certain limitations. These limitations include low thermal conductivity, high susceptibility to corrosion, and low thermal stability. These factors can affect the overall performance and durability of LHTES systems, necessitating

careful consideration and selection of suitable PCMs for specific applications. The inefficient thermal energy transfer caused by low thermal conductivity can result in slower heat absorption or release, impacting the overall performance and effectiveness of the LHTES system. It becomes crucial to address this issue and explore strategies to enhance the thermal conductivity of PCMs to ensure optimal charging. In the literature, various techniques have been explored to enhance the performance of LHTES systems:

1. The addition of high-thermal-conductivity materials to PCMs [8]: This method involves incorporating materials with high thermal conductivity, such as metal nanoparticles [9], carbon nanotubes [10], and graphite nanoplates [11], into the PCM matrix. By doing so, the overall thermal conductivity of the composite material is increased, leading to improved heat transfer and enhanced performance of the LHTES system.
2. The insertion of extended surfaces into PCMs [12,13]: Extended surfaces, such as fins or heat transfer plates, are inserted into the PCM to increase the effective surface area for heat transfer. This helps enhance the heat transfer rate between the PCM and the surrounding environment, resulting in an improved performance of the LHTES system.
3. Embedded heat pipes [14,15]: Heat pipes, which are highly efficient heat transfer devices, can be embedded within the PCM. These heat pipes facilitate heat transfer over longer distances, allowing for more efficient heat exchange and an improved thermal performance of the LHTES system.
4. The utilization of porous materials combined with PCMs [16,17]: Porous materials, including metallic foams, can be combined with PCMs to create composite structures. These porous materials provide additional surface area and interconnected pathways for heat transfer, enhancing the overall thermal conductivity and performance of the LHTES system.

These techniques represent some of the approaches that have been investigated in the literature to enhance the performance of LHTES systems. By implementing these techniques, researchers aim to overcome the limitations associated with PCMs and optimize the efficiency of thermal energy storage.

In the experimental investigation conducted by Aqib et al. [10], the focus was on studying the effect of incorporating nanoparticles, specifically alumina and carbon nanotubes, on the performance of LHTES systems. The study's findings revealed that adding either alumina or carbon nanotubes resulted in an increase in the maximum temperature attained by the system. Furthermore, the investigation indicated that among the nanoparticles studied, a concentration of 6 wt% of nanosized carbon tubes resulted in the highest increase in the peak temperature compared with the alumina nanoparticles. Al-Waeli et al. [8] experimentally investigated the impact of utilizing nanofluid and nano-PCM in a photovoltaic thermal (PVT) system. The study's objective was to examine how the integration of nanofluid and nano-PCM can influence the system's thermal and electrical efficiencies. Through their experiments, the authors demonstrated that the proposed PVT system, incorporating nanofluid and nano-PCM, improved thermal and electrical efficiencies.

Motahar et al. [18] conducted an experimental study to investigate the influence of TiO_2 nanoparticles on the solidification process of PCMs. The experimental findings revealed that the inclusion of TiO_2 nanoparticles in the PCM had a noticeable impact on the solidification process. The authors observed that as the mass fraction of nanoparticles increased, the solidification volume of the PCM also increased. In their numerical investigation, Kant et al. [19] examined the impact of incorporating graphene nanoparticles into PCMs for thermal energy storage applications. The findings of their study demonstrated that the addition of nanoparticles resulted in an increase in the melting rate of the PCM. Furthermore, the numerical investigation revealed that the incorporation of nanoparticles led to a reduction in convection heat transfer inside the large enclosure.

Arshad et al. [12] conducted a 2D numerical study to analyze the impact of embedded fins in a PCM on the cooling performance of electronic devices. The authors showed that the melting time of the PCM depended strongly on the fins' thickness. The results suggested

that increasing the thickness of the fins resulted in a longer melting time for the PCM. This implies that the presence of thicker fins hindered the heat transfer process, leading to a slower melting rate. On the other hand, reducing the thickness of the fins enhanced the heat transfer capabilities, thereby decreasing the melting time of the PCM. A numerical investigation was conducted by Bondareva and Sheremet [20] to analyze the combined flow and heat transfer phenomenon of a finned copper profile integrated within a heat storage system using PCMs. The results of their study indicated that the duration needed for the PCM to melt completely is influenced by the dimensions of the fins, including their length and width. The impact of different pin fin heat sink designs (triangular, rectangular, and circular) on the cooling of an electronic device with PCMs was experimentally examined by Ali et al. [13]. The results of their investigation revealed that the triangular pin fins exhibited the highest efficiency level among the tested configurations.

The performance of heat pipe solar collectors integrated into an LHTES system was experimentally examined by Essa et al. [21], with a specific focus on the impact of using helical fins versus conventional fins. The findings of their study showed that the implementation of helical fins resulted in superior thermal performance when compared with conventional fins. Mahdavi et al. [9] numerically investigated the combined influence of nanoparticles and heat pipes on the thermal performance of LHTES systems. The study revealed that the utilization of heat pipes significantly impacted the performance of LHTES systems compared with the dispersion of nanoparticles.

The literature review shows that no study has investigated the effect of different configurations of metal fins on the thermal performance of a semi-cylindrical LHTES system. The primary goal of this study is to conduct a numerical analysis of various configurations of an LHTES system, taking into consideration both pure PCMs and NePCMs. The investigation focuses on evaluating the influence of graphite nanoparticles at different mass fractions. Furthermore, various designs of finned structures are assessed to identify an optimal fin-enhanced configuration for the energy storage system. The configuration with the shortest charging time is selected for further enhancement using nano-additives. Additionally, a comprehensive analysis and discussion are carried out regarding the distribution of energy storage (sensible or latent) in different storage system components, including the PCM, fins, and walls, providing detailed insights into their respective contributions.

2. Problem Definition

Figure 1 depicts various configurations of the LHTES system containing the NePCM. As shown, warm water with a temperature T_{HTF} enters the semicircular channel and transfers a portion of its thermal energy to the solid NePCM via the copper separators. Consequently, the NePCM undergoes a phase change from solid to liquid as it absorbs thermal energy from the warm water. It is important to highlight that in each configuration, the total volume of the fins remains constant. This implies that as the length of the fins changes from one case to another, the thickness of the fins also varies accordingly. This ensures that the overall volume occupied by the fins remains constant throughout the different configurations. Additionally, it should be noted that the vertical fin (middle fin) remains unaltered in cases 2 through to 10. The additives, which are uniformly mixed with the base medium (pure 1-Tetradecanol), include nanosized graphite plates. Tables 1 and 2 provide detailed specifications of the materials involved in the LHTES unit. These tables outline the specific characteristics and properties of the various materials utilized within the system, providing valuable information about their composition, thermal conductivity, phase change temperatures, and other relevant parameters.

The NePCM container in the LHTES unit has a radius of 50 mm. Additionally, a copper separator is attached to the channel with a thickness of 2 mm. The cross-sectional size of the channel, through which the heat transfer fluid (HTF) flows, is $W = 3$ mm. The volume changes of the NePCM during the melting process can be disregarded.
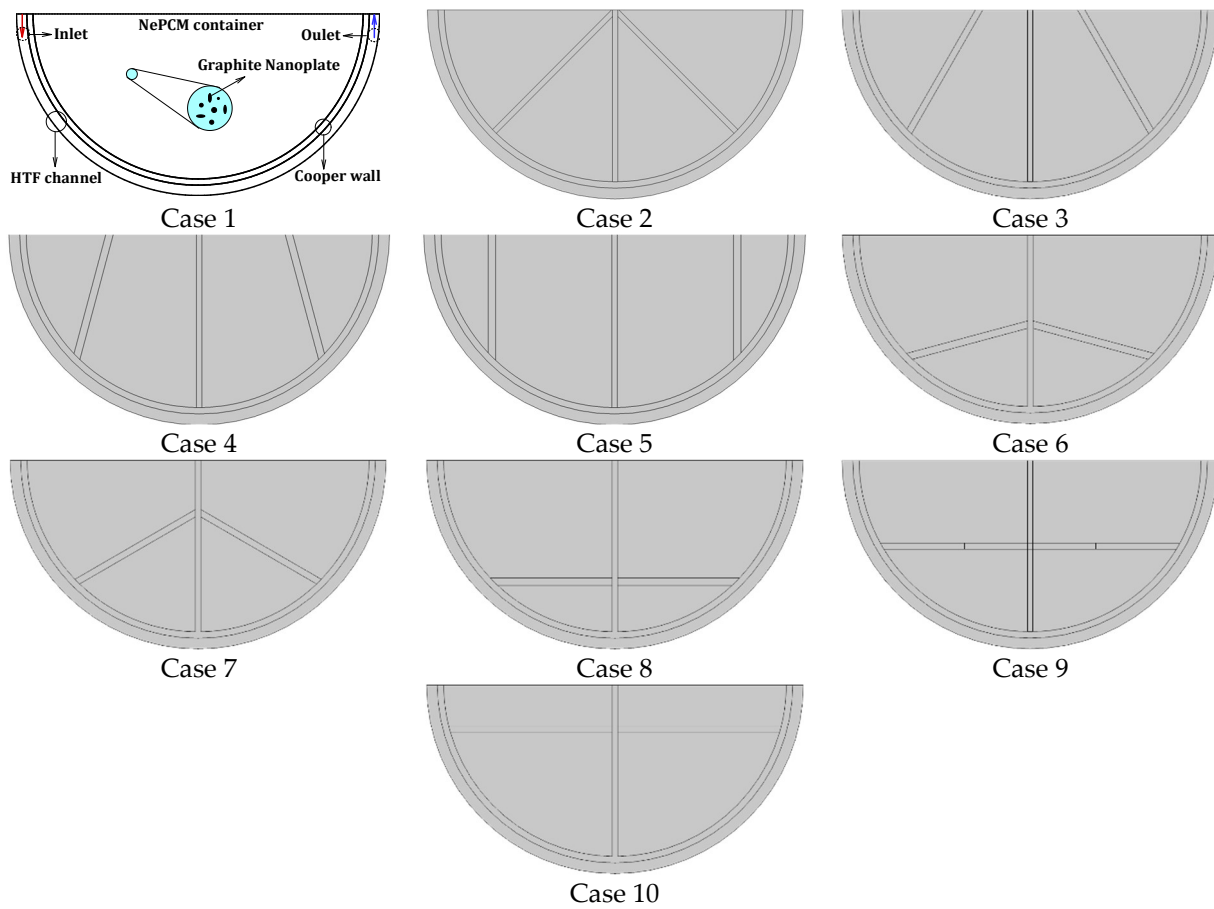
Figure 1. Schematic view of the problem and the design of the finned cases.

The Reynolds number of the HTF based on the thermo-physical properties of the HTF (Table 1), $v_{HTF} = 0.01$ m/s, and the cross-sectional size of the channel ($W = 3$ mm) is 42.28. Additionally, the Rayleigh number for NePCM with the mass fraction 3% based on the radius of the semi-cylindrical LHTES unit is 4.19×10^5. Based on the Reynolds and Rayleigh numbers, the flow regimes within the HTF channel and the chamber housing the molten liquid are characterized as laminar.

Table 1. Thermo-physical properties of water and copper separators [22,23].

Properties	$\rho(\text{kgm}^{-3})$	$\mu(\text{Nsm}^{-2})$	$c_p(\text{Jkg}^{-1}\text{K}^{-1})$	$\lambda(\text{Wm}^{-1}\text{K}^{-1})$
Water	993.7	0.705×10^{-3}	4178	0.623
Copper	8900	-	386	401

3. Governing Equations

3.1. Governing Equations of the Velocity and Temperature Fields of the NePCM Domain

To model the progressive melting front, the well-known enthalpy–porosity approach with a fixed mesh is used. Considering the assumptions presented in Section 2, the equations describing the melting flow can be derived as the following [24,25]:

(I)   Continuity equation

$$\nabla \cdot \vec{u} = 0 \tag{1}$$

(II) Momentum equations

$$\rho_{lNePCM}\frac{\partial u}{\partial t} + \rho_{lNePCM}\left(\vec{u}\cdot\nabla\right)u = -\frac{\partial p}{\partial x} + \nabla\cdot\left(f(\mu_{NePCM},T)\nabla u\right) + F_{mx} \tag{2}$$

$$\rho_{lNePCM}\frac{\partial v}{\partial t} + \rho_{lNePCM}\left(\vec{u}\cdot\nabla\right)v = -\frac{\partial p}{\partial y} + \nabla\cdot\left(f(\mu_{NePCM},T)\nabla v\right) + F_{by} + F_{my} \tag{3}$$

To suppress the velocity components in the solid NePCM region, volume forces F_{mx} and F_{my} are imposed on the momentum equations as follows [26]:

$$\left(F_{mx},\ F_{my}\right) = -\frac{B_{mush}(1-\eta(T))^2}{\eta^3(T)+\varepsilon}(u,v) \tag{4}$$

The values of B_{mush} and ε are 5×10^5 and 10^{-3}. $H(T)$ is defined as follows [26]:

$$\eta(T) = \begin{cases} 0 & T \leq T_{me} - 0.5\Delta T_{me} \\ \frac{2(T-T_{me})+\Delta T_{me}}{2\Delta T_{me}} & T_{me} - 0.5\Delta T_{me} < T < T_{me} + 0.5\Delta T_{me} \\ 1 & T \geq T_{me} + 0.5\Delta T_{me} \end{cases} \tag{5}$$

$\eta(T)$ can also be employed to introduce the overall dynamic viscosity of the NePCM as follows:

$$f(\mu_{NePCM},T) = \mu_{NePCM}(1+\eta(T)) \tag{6}$$

Moreover, the buoyancy force resulting from the gravity acceleration is:

$$F_{by} = -\rho_{lNePCM}g\beta_{lNePCM}(T - T_{me}) \tag{7}$$

Table 2. Thermo-physical properties of NePCM samples at various mass fractions of nanosized graphite plates [27].

Properties	0.0 wt%	0.50 wt%	1.0 wt%	3.0 wt%
$\rho_{sNePCM}\left(\text{kgm}^{-3}\right)$	891.4	894.1	896.9	907.9
$\rho_{lNePCM}\left(\text{kgm}^{-3}\right)$	821.6	824.3	826.9	837.6
$\mu_{NePCM}(\text{mPas})$	13.23	23.45	59.5	194.01
$c_{p,sNePCM}\left(\text{Jkg}^{-1}\text{K}^{-1}\right)$	2040	2020	1990	1910
$c_{p,lNePCM}\left(\text{Jkg}^{-1}\text{K}^{-1}\right)$	2360	2330	2300	2190
$T_{me}\ (\degree\text{C})$	37	37	37	37
$L\left(\text{kJkg}^{-1}\right)$	227.8	219.5	212.2	183.5
$\beta_{lNePCM}\left(\text{K}^{-1}\right)$	0.001018	0.001018	0.001008	0.000987
$\lambda_{sNePCM}\left(\text{Wm}^{-1}\text{K}^{-1}\right)$	0.252	0.350	0.451	0.540
$\lambda_{lNePCM}\left(\text{Wm}^{-1}\text{K}^{-1}\right)$	0.159	0.180	0.260	0.320

(III) Energy equation

$$\rho_{NePCM}c_{p,NePCM}\frac{\partial T}{\partial t} + \rho_{NePCM}c_{p,NePCM}\left(\vec{u}\cdot\nabla\right)T = \nabla\cdot\left(\lambda_{NePCM}\nabla T\right) \tag{8}$$

where

$$\lambda_{NePCM}(T) = \lambda_{lNePCM} + (1-\eta(T))\lambda_{sNePCM} \tag{9}$$

$$\rho_{NePCM}(T) = \rho_{lNePCM} + (1 - \eta(T))\rho_{sNePCM} \tag{10}$$

$$c_{p,NePCM} = c_{p,sNePCM} + \eta(T)\left[c_{p,lNePCM} - c_{p,sNePCM}\right] + L_{NePCM}D(T) \tag{11}$$

in which D (T) is a Gaussian function as follows:

$$D(T) = \frac{exp\left(\frac{(T - T_{me})^2}{\left(\frac{\Delta T_{me}}{4}\right)^2}\right)}{\sqrt{\frac{\pi}{\left(\frac{\Delta T_{me}}{4}\right)^2}}} \tag{12}$$

3.2. Governing Equations of the Velocity and Temperature Fields for Water Flow in the Channel

The governing equations of the velocity and temperature of the heat transfer fluid inside the channel are as follows:

(I)   Continuity equation

$$\nabla \cdot \vec{u} = 0 \tag{13}$$

(II) Momentum equations

$$\rho_{HTF}\frac{\partial u}{\partial t} + \rho_{HTF}\left(\vec{u} \cdot \nabla\right)u = -\frac{\partial p}{\partial x} + \nabla \cdot (\mu_{HTF}\nabla u) \tag{14}$$

$$\rho_{HTF}\frac{\partial v}{\partial t} + \rho_{HTF}\left(\vec{u} \cdot \nabla\right)v = -\frac{\partial p}{\partial y} + \nabla \cdot (\mu_{HTF}\nabla v)$$

(III) Energy conservation

$$(\rho c_p)_{HTF}\frac{\partial T}{\partial t} + \left(\rho c_p\right)_{HTF}\left(\vec{u} \cdot \nabla\right)T = \nabla \cdot (\lambda_{HTF}\nabla T) \tag{15}$$

3.3. Energy Conservation for the Copper Wall and Fins

The equation describing energy conservation in the copper wall and fins is as follows:

$$(\rho c_p)_c\frac{\partial T}{\partial t} = \nabla \cdot (\lambda_c\nabla T) \tag{16}$$

3.4. Boundary Conditions

The outer border of the half-cylinder is well insulated, and the no-slip boundary condition is valid on the channel surfaces. Therefore, the mathematical form of the thermal and hydro-dynamics boundary conditions on these bounds is expressed as

$$u = 0, \; v = 0 \; and \; \frac{\partial T}{\partial n} = 0 \tag{17}$$

At the interface of the copper wall and the channel of heat transfer fluid, the conditions are

$$u = 0, \; v = 0 \; and \left(\frac{\lambda\partial T}{\partial n}\right)_c - \left(\frac{\lambda\partial T}{\partial n}\right)_{HTF} = 0 \tag{18}$$

The thermal and hydro-dynamic conditions at the channel inlet are

$$u_{HTF} = 0.0, \; v_{HTF} = 0.01 \; m/s, \; T_{HTF} = 50°C \tag{19}$$

The initial condition at the whole domain is as follows:

$$u = 0, \ v = 0 \ and \ T - 25^\circ\text{C} = 0 \tag{20}$$

At the interface of phase change material and copper fins, we have

$$u = 0, \ v = 0 \ and \ \left(\frac{\lambda \partial T}{\partial n}\right)_c - \left(\frac{\lambda \partial T}{\partial n}\right)_{NePCM} = 0 \tag{21}$$

Furthermore, the diameter of the cylinder as an external wall is thermally insulated and the no-slip boundary condition is valid on it:

$$\left(\frac{\lambda \partial T}{\partial y}\right)_{NePCM} = 0, \ u = v = 0 \tag{22}$$

3.5. Characterizing the Stored Energy

The total stored energy in the LHTES system, including the sensible and latent components, is as follows:

$$
\begin{aligned}
&Total\ Stored\ Energy \\
&= \overbrace{\int_{A_{NePCM}} \rho_{NePCM} C_{p,NePCM}(T - T_0)\, dA}^{Sensible\ energy\ stored\ in\ the\ NePCM} \\
&+ \overbrace{\int_{A_{NePCM}} \rho_{NePCM} L_{NePCM} dA}^{Latent\ energy} + \underbrace{\int_{A_{fins}} \rho_{fin} C_{p,fin}(T - T_0)\, dA}_{Sensible\ energy\ stored\ in\ the\ copper\ wall\ and\ fins}
\end{aligned}
\tag{23}
$$

The melted volume fraction (MVF) of NePCM is defined as follows [28]:

$$MVF(t) = \left[\int_A \eta(T) dA\right] A^{-1} \tag{24}$$

At the end, charging power as a measure of the system performance parameter is calculated as follows:

$$Charging\ power = \frac{Total\ Stored\ Energy}{t(s)} \tag{25}$$

4. Employed Numerical Method, Mesh Independence Test, and Validation

Based on the enthalpy–porosity approach, the NePCM region is modeled by taking into consideration the modified energy and momentum source terms. In the analysis, we treat the phase transition zone as a porous medium, representing it as a mushy zone with porosity defined by the liquid fraction $\eta(T)$. Through the mushy zone, a high-velocity gradient is developed since both solid and liquid NePCMs coexist. Moreover, a slight difference between the solidification and melting temperatures is considered (ΔT_{me}). The non-linear governing equations are solved using the finite element approach within version 5.6 of the COMSOL Multiphysics computational fluid dynamics module [29]. Since the problem is transient, one of the best implicit methods is employed, which is the free step backward differentiation formula. The coupled algebraic system is solved using the iterative parallel direct solver [30], coupled with the Newton method. The convergence plot is monitored, and the process continues until the residual error reaches 10^{-6}. A damping factor of 0.8 is utilized in the iterative Newton approach to prevent divergence. Figure 2 shows a convergence plot of the coupled numerical solution.
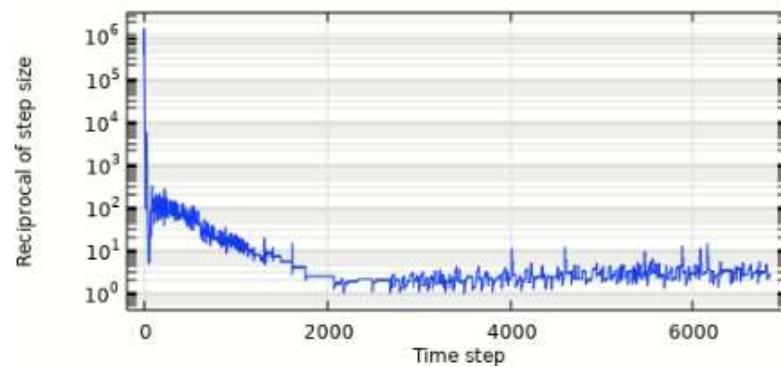
Figure 2. Convergence plot of the coupled numerical solution.

Recognizing the importance of the mesh density in ensuring the accuracy of numerical results, meticulous grid independence tests were conducted. To achieve this objective, the corresponding MVF for the five different mesh densities, as presented in Table 3, are compared to ensure that the accuracy of the iterative solution is maintained (see Figure 3). It can be noticed that all cases are consistent. However, a slight difference is seen for Case (I), when a relatively small grid size is considered. Consequently, Case (III) (7043 elements) is chosen to retain an acceptable accuracy while minimizing calculation cost as much as possible.

Table 3. Grid test cases.

Cases	Case I	Case II	Case III	Case IV	Case V
Number of elements	1635	4050	7043	10,632	14,926
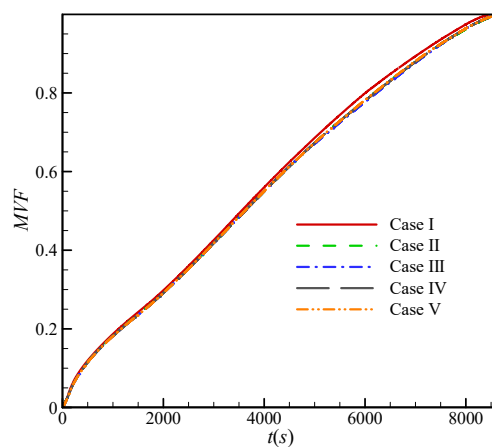
Figure 3. Dependency of the MVF on the mesh size.

Validating the current model's findings is crucial for quality and reliability. To validate the findings of the current model, both experimental and numerical data from prior research [31] were compared to the predictions of the current model. Kamkari et al. [31] used computational and experimental approaches to study PCM melting within a rectangular chamber. As demonstrated in Figure 4, the numerical and experimental data for the liquid fraction contours during PCM melting for $Ra = 8.3 \times 10^8$ at different time intervals (10–20–30–40 min) were successfully reproduced in the present model, which indicates its great consistency with the literature. It is worth noting that Ra is the Rayleigh number and is defined as $Ra = \frac{\rho_{lPCM} g \beta_{lPCM}(T_w - T_{me}) H^3}{\mu_{lPCM} \alpha_{lPCM}}$. Here, ρ_{lPCM} is the density of the liquid PCM, β_{lPCM} is the thermal expansion coefficient of the liquid PCM, T_w is the temperature of the hot wall, H is the height of the enclosure, μ_{lPCM} is the dynamic viscosity, and α_{lPCM} is the

thermal diffusivity of the liquid PCM. The values of these thermo-physical properties can be found in [31].
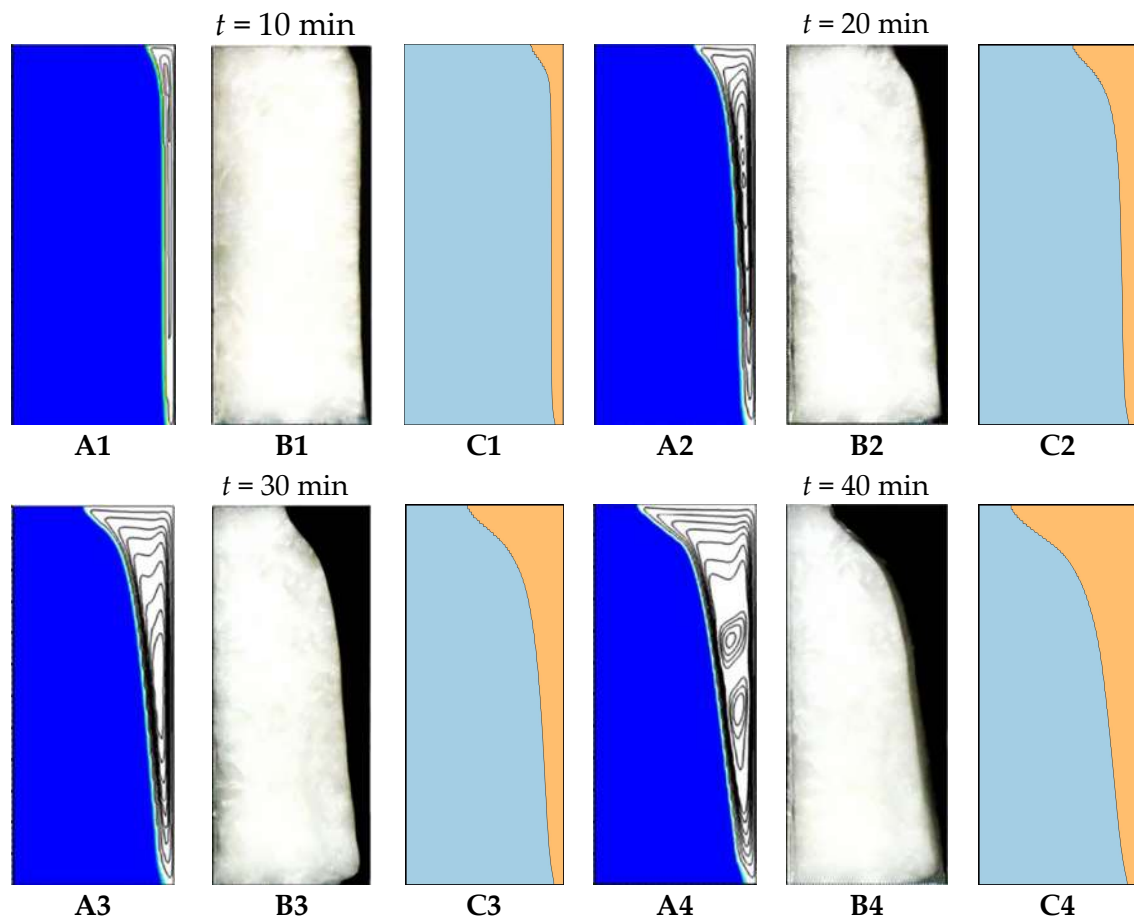
$t = 10$ min $t = 20$ min

$t = 30$ min $t = 40$ min

Figure 4. Comparison between the melting fields available in [31] and those obtained by the present study; (**A1**–**A4**): numerical results [31], (**B1**–**B4**): experimental results in [31], and (**C1**–**C4**): the present study.

5. Results and Discussion

The results of the current study are presented in two separate sections. In the first section, the melting process of the ten cases with different fin configurations is studied and discussed. The second part is then devoted to the nano-enhancement of the case with the optimum result (out of the finned cases) with graphite nanoplatelets (GNPs).

5.1. Finned Configurations

The contours of melt fraction, velocity, and temperature of the PCM for the above-discussed cases at three different times of 1000, 3000, and 5000 s of simulation are shown in Figures 5–7. The HTF flows through the curved channel attached to the storage and melts the PCM. The HTF has a higher temperature at the entrance, and its temperature decreases as it transfers its thermal energy to the PCM via the wall. Hence, for all cases, the melting process proceeds faster near the HTF entrance area. As discussed earlier, excluding Case 1, the volume of the employed fins in all the cases is constant, and hence, the volume of the phase change materials is set as constant for Cases 2–10 to ease the assessment of the role of fin configuration.
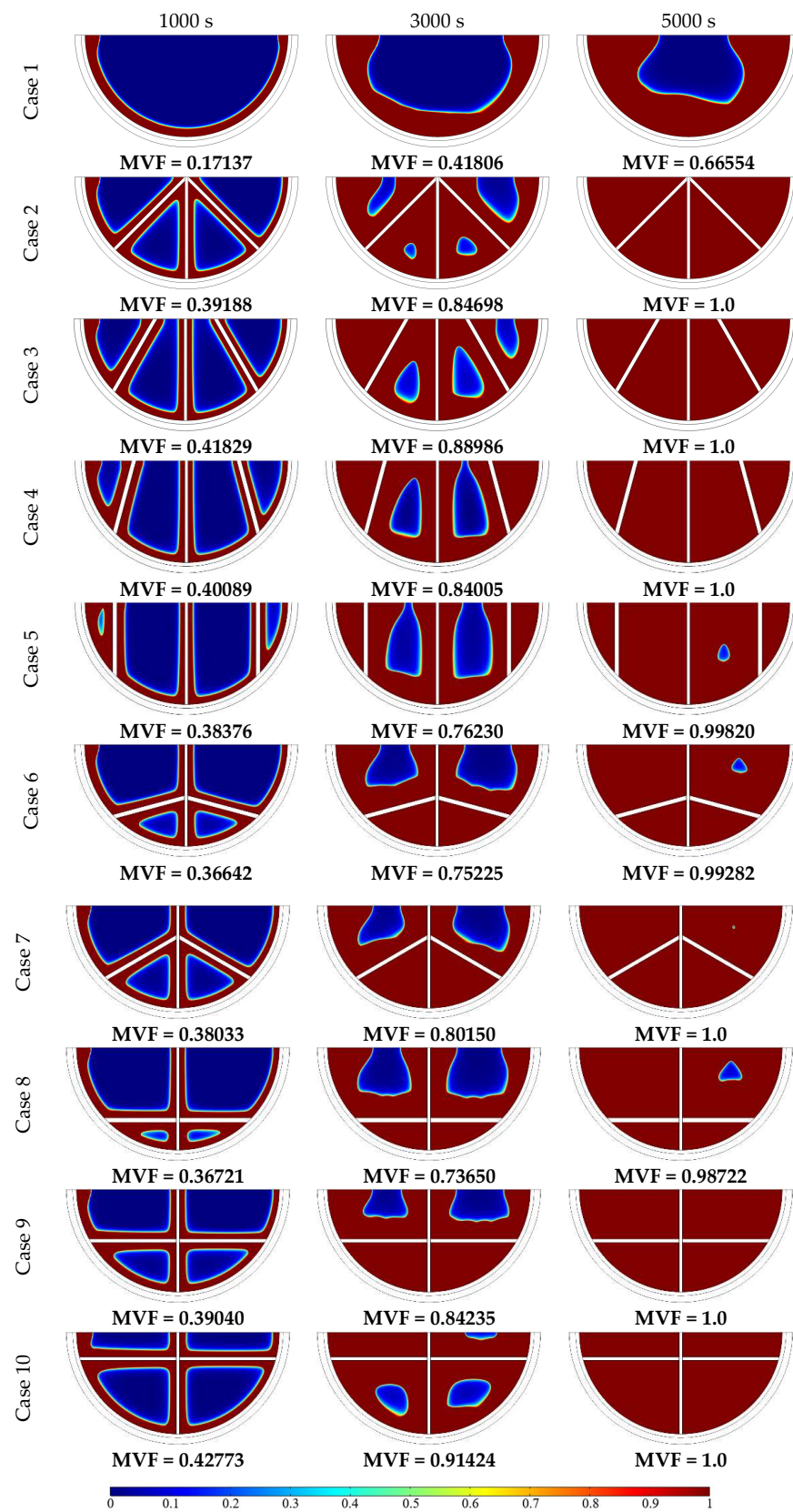
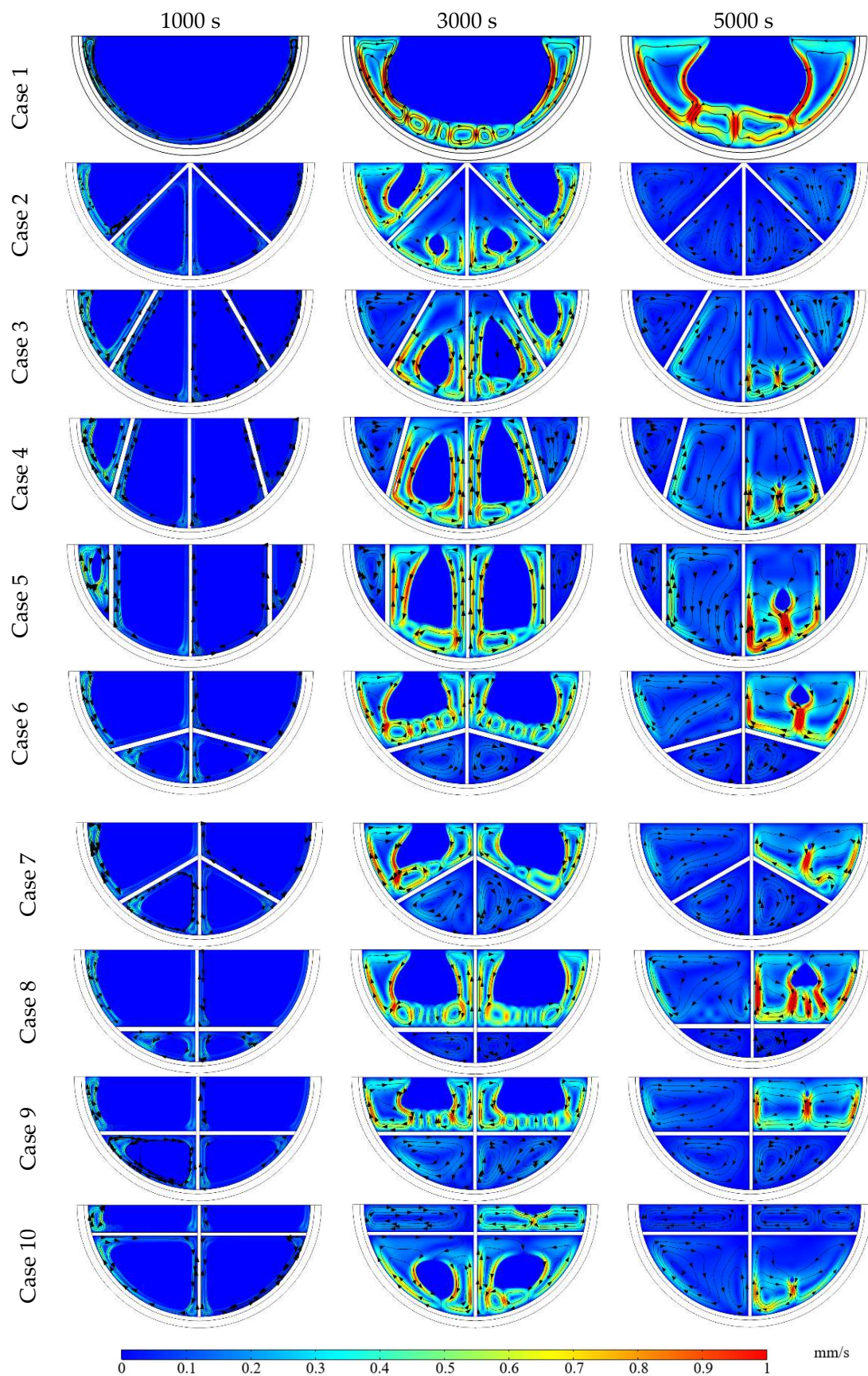**Figure 5.** Melt fraction contours for the studied cases at different simulation times.

Figure 6. Velocity magnitude contours and streamlines of the liquid PCM for the studied cases at different simulation times.
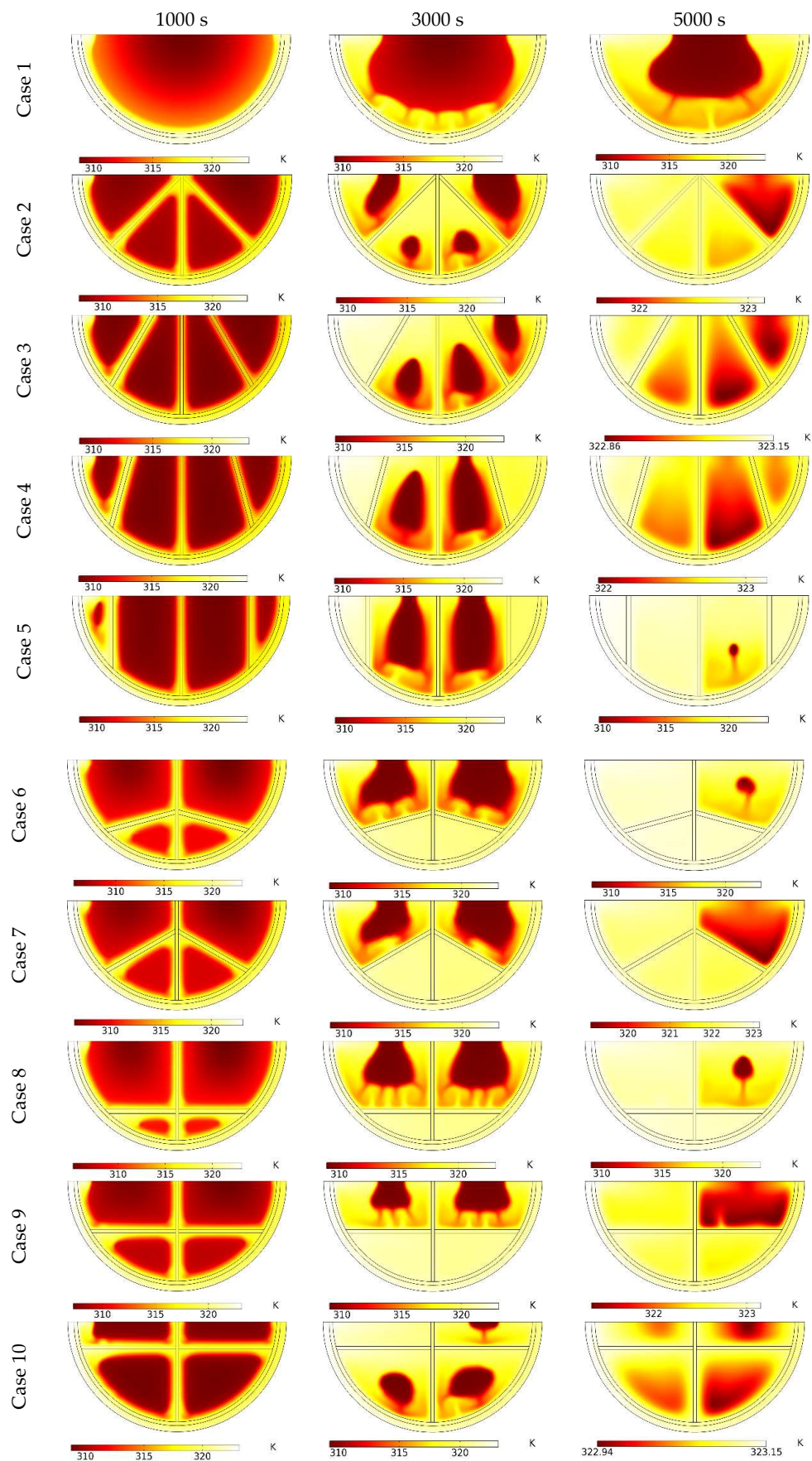
Figure 7. Temperature contours of the PCM for the studied cases at different simulation times.

Case 1 has no fin, and hence, a lower melting rate is anticipated due to the low thermal conductivity of the Tetradecanol (Table 1). All the other cases have a higher melting rate compared with the unfinned case. As discussed before, the vertical fin, called the fixed fin hereafter, in the middle of the storage remains unchanged and divides the storage into two equal quarter cylinders. The locations of the other two fins (called variable fins) are therefore quite important to improving the storage's melting rate, as they divide each quarter cylinder into two non-equal smaller storages. Hence, the angle and vertical placement of the fins have been varied (shown in Cases 2–10) to assess the proper configuration during the charging process of the storage.

As shown in Figure 5, after 3000 s of charging, in most cases, the PCM near the horizontal wall remains unmelted, as the mentioned wall is adiabatic. In other words, the attachments of the other fin (in each quarter cylinder) can determine the charging time of the storage. The angle of the variable fins is changed from vertical (Case 5) to inclined (Cases 2, 3, 4, 6, and 7) and finally vertical (Cases 8, 9, and 10) to evaluate the role of the angle of the fin. According to Figure 6, the velocity magnitude at the initial stages of the charging is low, indicating that the conduction mode of the heat transfer mainly governs the charging process. This can also be understood from the temperature contours (Figure 7). The role of fin placement can be easily seen in Figure 7, as it elevates the temperature around it through conducting thermal energy to the PCM. With the progression of the charging, the convection mechanism increases, and the magnitude of velocity (Figure 6) and temperature (as per Figure 7) of the liquid PCM increases.

Using a symmetric fin configuration (Case 2) can significantly improve the melting process (compared with Case 1). However, the charging process in the portions in the vicinity of the insulated top wall is obviously lower than in the remaining portions (see the blue region in Figure 6 and the bulk red region in Figure 7, showing the not melted PCM). To address this issue, the variable fins in Cases 3, 4, and 5 were directly attached to the insulated wall to conduct heat from the copper wall to the PCM near the insulated wall. This strategy, as can be seen in Figures 6 and 7, leads to a more significant segment on the left- and right-hand sides of the fixed fin, increasing the overall melting time of the whole storage.

In Cases 6–10, the variable fins are attached to the fixed fin. The variable fins are inclined for Cases 6 and 7, while for Cases 8–10, they are attached horizontally to the fixed fin. The upper portion of the storage near the insulated wall remains unmelted. The attachment height has been changed for the last three cases. It is evident that by decreasing the distance between the variable fins and the insulated surface, according to Figure 7, the overall temperature of the PCM increases, leading a reduction in the amount of solid PCM, and an enhancement in the melting rate.

Figure 8a,b illustrate the time variation of the stored energy and the liquid fraction of the PCM during the charging process. Case 1 (without fin) has the lowest melting rate, and after 5000 s of charging, only 60% of the PCM in the storage is charged. Case 10 has the highest charging rate throughout the melting process. The variable fins in Case 10 are closer to the insulated wall, so a higher amount of heat is conducted to the PCM. Figure 9 depicts the detail of the different types of thermal energy stored in the PCM (either latent or sensible) and the fins (sensible). It is clear that the stored energy in the storage is mainly in the form of latent energy.

The sensible energy in the PCM increases very sharply at the beginning of the charging process as walls transfer the heat and the fins store this in the form of sensible heat (the initial temperature of the PCM is below the melting point, as shown in Equation (20) and Table 2). The rate of storing sensible energy decreases after about 600 s, as the energy is mainly stored in the form of latent heat. After around 2600 s of simulation, the rate of sensible energy accumulation increases again, as most of the PCM has been melted (about 70%, as shown in Figure 8b), and the rate of energy storage in the form of latent heat shows a downward trend (Figure 9a).
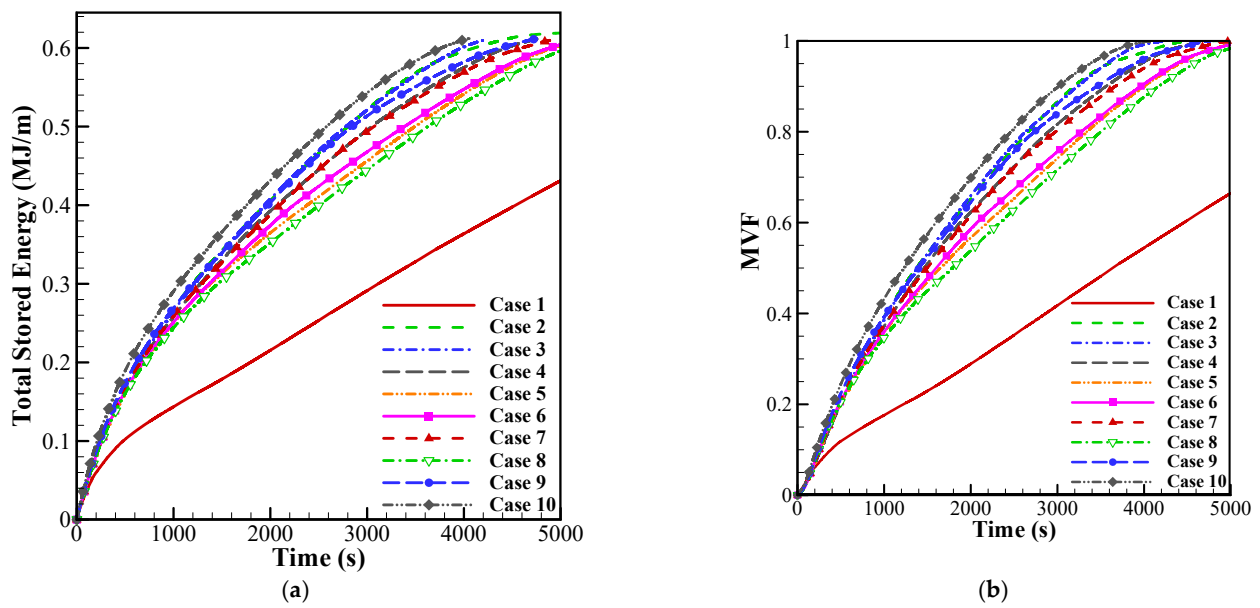
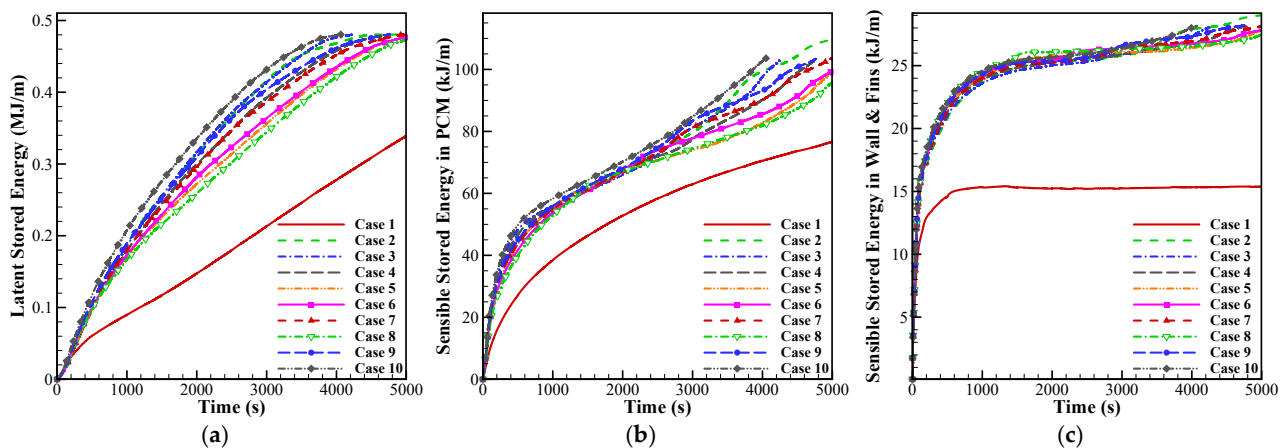**Figure 8.** (**a**) Total energy stored and (**b**) liquid fraction for Cases 1–10.

Figure 9. Details of the total energy stored in the storage for cases 1–10: (**a**) latent heat stored in PCM, (**b**) sensible heat stored in PCM, and (**c**) sensible heat stored in the wall and fins.

The sensible energy in the fins (Figure 9c) remains approximately constant after a short time of the charging process has passed, indicating that the (average) fins' temperature remains roughly constant due to their high conductive heat transfer feature. Note that at the late stages of the charging process, where most of the PCM is melted, the sensible energy of the fins slightly increases, meaning that the (average) fins' temperature increases when the storage is almost charged (80% or above, according to Figure 8b).

Figure 10 shows the charging power for Cases 1–10. The charging power at the beginning of the charging process is very high, mainly because of the temperature difference between the HTF and the storage (PCM and fins). As time elapses, the charging power decreases steadily. As the melting rate of Case 10 is higher than that of the other cases, a higher charging power is also anticipated for this case. In addition, a closer look at Figure 10 reveals that although Case 9 has the second-highest charging power after around 900 s of the charging process, at the late stages of charging, the charging power of Case 3 overtakes Case 9. The presented results also confirm that attention should be paid when designing an LHTES, as it might undergo a partial charging process. For more details about the partial/full charging process of the LHTES, interested readers are referred to Hashem Zadeh et al. [32].
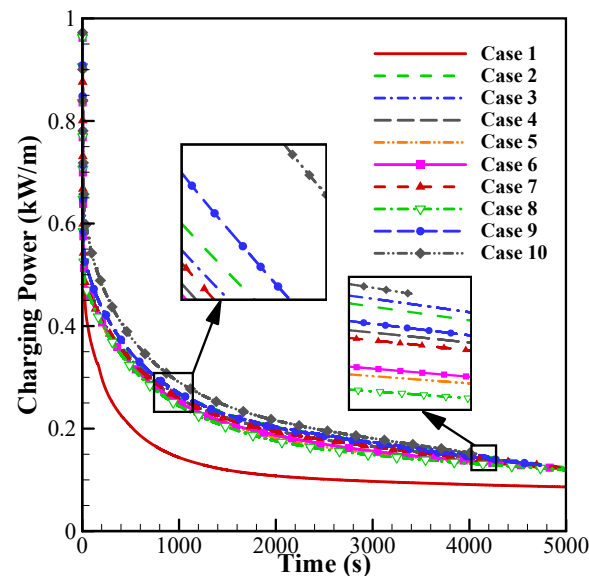
Figure 10. Instantaneous charging power for Cases 1–10.

5.2. Nano-Enhancing the Best Case with GNP

In the previous section, the role of different configurations of the fins on the charging process of the storage was studied and analyzed in detail. It was found that Case 10 has the highest charging power. In this part, we have surveyed the effects of graphite nanoplates on the melting characteristics of the selected case (i.e., Case 10).

Figures 11 and 12 compare, respectively, the melting fraction contours and temperature files of the nano-enhanced cases with the case of a pure PCM. It is evident that the melting rate and temperature of the PCM significantly increases when the nano-enhanced particles are added to the PCM. Adding nano-additives to the PCM slightly decreases the total capacity of the storage, as a portion of the storage is occupied by the nano-additives. On the other hand, with dispersing nanoparticles, the effective thermal conductivity of the medium increases considerably (as presented in Table 2, only by adding 3% of the analyzed nano-additive, the thermal conductivity of the solid nano-PCM almost doubles). As a result, a higher amount of thermal energy can be transferred and the melting rate increases.

Figure 13 shows the total amount of thermal energy stored in the LHTES and the liquid portion of the PCM during charging. Figure 13a shows that the total thermal energy stored accelerates with dispersing nanosized particles. However, as discussed before, the total amount of energy decreases with increasing nanoparticle concentration. It is evident that the liquid fraction of the nano-enhanced PCM increases as the concentration of the nanoparticles increases (Figure 13b).

Figure 14 presents different forms of thermal energy in the storage. By increasing the GNP concentration, the sensible form of energy in the fins, wall, and the nano-PCM increases. Concerning the nano-enhanced PCM, this is plausible, as the energy stored in the nanoparticles is only sensible energy and increases as the mass fraction of the nanoparticles increases.

Figure 15 shows the instantaneous charging power of the cases enhanced with the GNP nanoparticle. As discussed before, the charging power increases by dispersing the GNP nanoparticles, meaning that the storage charges faster. Nonetheless, as can be seen, the instantaneous charging power of the storage (time-based charging power defined in [32]) may be non-monotonic and vary during the charging process. In other words, the storage's full charging power is higher for script phi, of which $\varphi = 3.0\%$. However, in terms of partial charging power, the charging power for the case of $\varphi = 1.0\%$ is slightly higher at the last stages of the charging process (the magnified area in Figure 15).
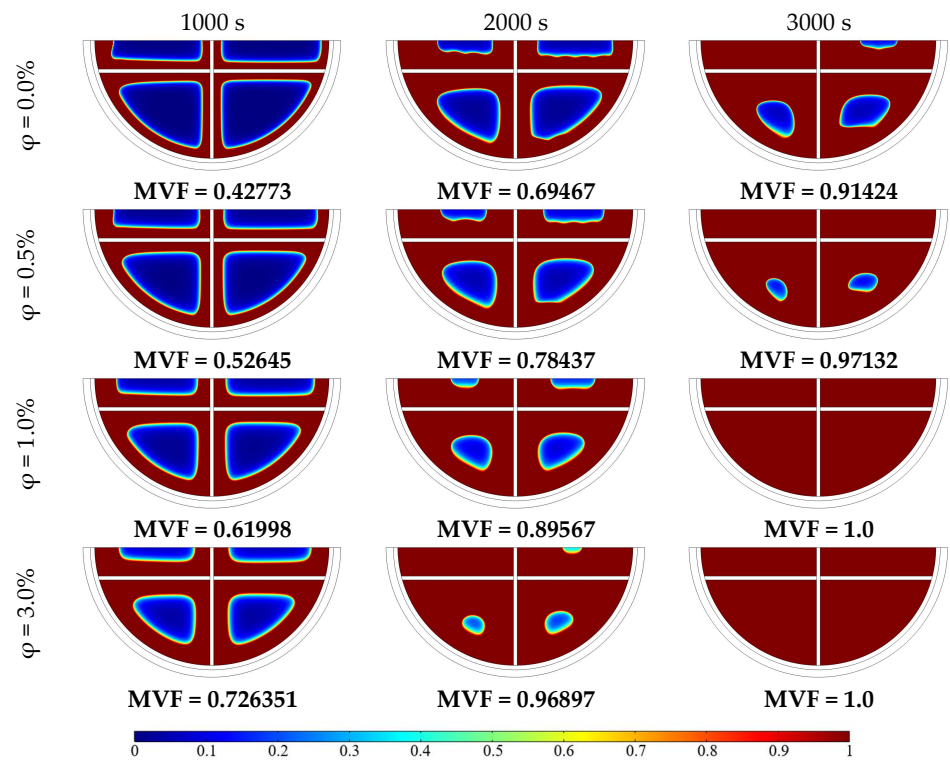
Figure 11. Melting fraction contours for the nano-enhanced PCM (Cases 10–13) at different simulation times.
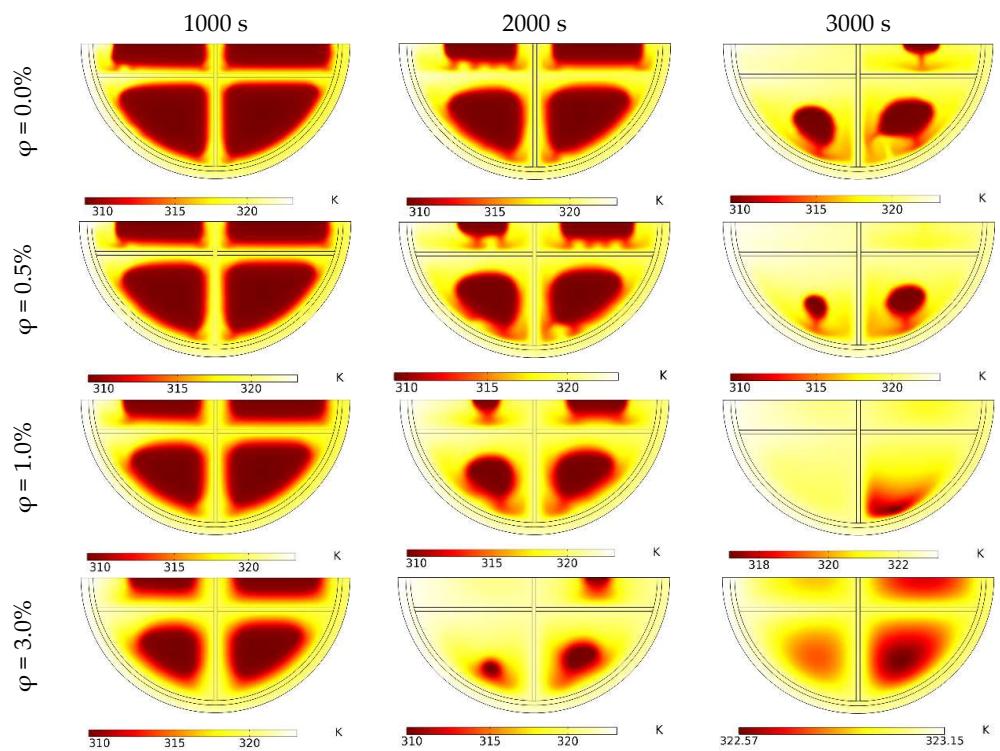

Figure 12. Temperature contours for the nano-enhanced PCM (Cases 10–13) at different simulation times.
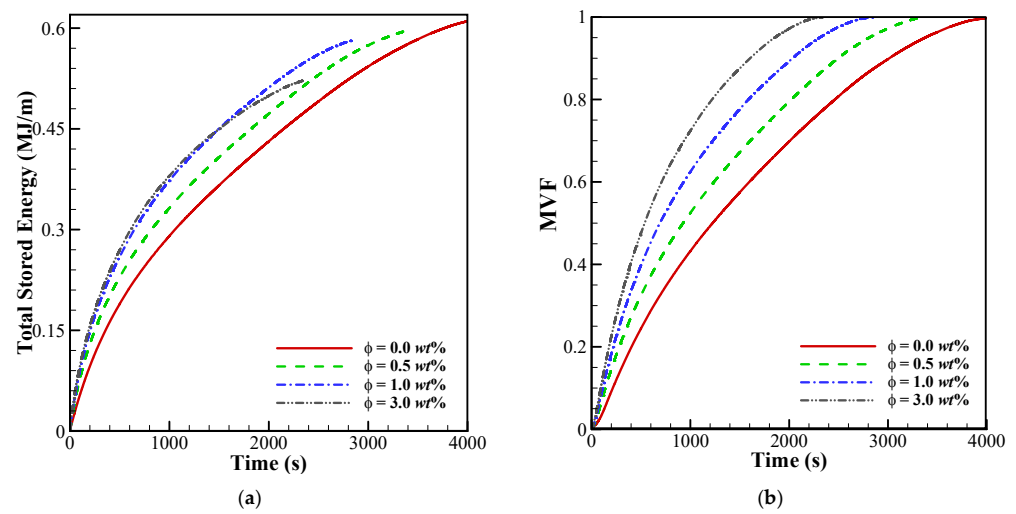
Figure 13. (**a**) Total energy stored and (**b**) liquid fraction for different mass fractions of GNP nanoparticles.
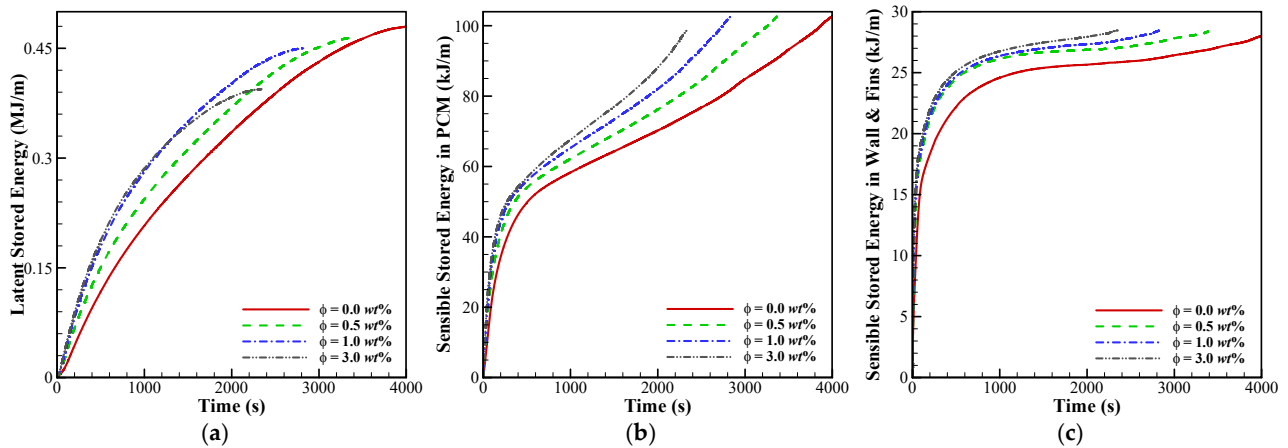

Figure 14. Details of the total energy stored in the storage for different concentrations of GNP nanoparticles: (**a**) latent heat stored in PCM, (**b**) sensible heat stored in PCM, and (**c**) sensible heat stored in the wall and fins.
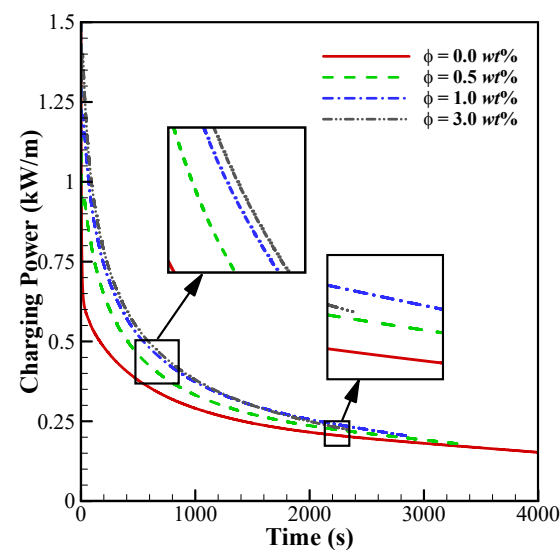

Figure 15. Instantaneous charging power for different concentrations of GNP nanoparticles.

6. Conclusions

The charging behavior of a half-cylinder-shaped latent heat thermal energy storage is studied. The storage medium is Tetradecanol. The results are divided into two sections. The first section selects ten different fin configurations (including horizontal, inclined, and vertical fins) for analysis. The volume of the fins for all the cases is kept constant for the sake of comparison. The second part selects the case with the highest charging power for nano-enhancement with graphite nanoplatelets (GNPs). The stored energy in the PCM/NePCM (sensible and latent heat) and the fins and walls (sensible heat) are discussed in detail. The outcomes of the two parts can be summarized as follows:

1. For the finned cases, the highest charging power can be achieved only when the variable fins are horizontally attached to the fixed fin and close to the insulated wall.
2. The sensible energy in the PCM increases very sharply at the beginning of the charging process and then decreases as the melting process starts. The sensible energy increases again when the storage charges to about 70%.
3. The sensible energy in the fins remains approximately constant after a short time of the charging process has passed, indicating that the (average) fins' temperature remains roughly constant.
4. Adding nano-additives to the PCM slightly decreases the total capacity of the storage, as a portion of the storage is occupied by the nano-additives. In addition, the total thermal energy stored (and the liquid fraction of the NePCM) accelerates with the dispersal of nanosized particles.
5. By increasing the concentration of the GNPs, the sensible form of energy in the fins, wall, and nano-PCM increases.
6. By dispersing the GNP nanoparticles, the charging power increases, meaning the storage charges faster.

To summarize, this study attempts to find out how the configuration of fins (for a constant volume of fins) in a half-cylinder LHTES can affect the charging process of storage. The case with minimum charging time was used for the nano-enhancement. In addition, although the full charging power of the storage is analyzed here, the results of the simulations confirm that the charging power of the LHTES system (as surveyed in our previous research) is non-monotonic, and the best case for full charging power may not necessarily work well during partial charging.

Nomenclature

Latin symbols

B_{mush}	Mushy zone parameter
c_p	Sensible heat capacity ($\mathrm{Jkg^{-1}K^{-1}}$)
$D(T)$	Gaussian function
F_{by}	Buoyancy force ($\mathrm{Nm^{-3}}$)
F_{mx}	Sink term in x-momentum equation ($\mathrm{Nm^{-3}}$)
F_{my}	Sink term in y-momentum equation ($\mathrm{Nm^{-3}}$)
g	Gravity acceleration ($\mathrm{ms^{-2}}$)
L	Latent heat ($\mathrm{kJkg^{-1}}$)
p	Pressure (Pa)
T	Temperature (K)
t	Time (s)
u	Velocity component in x direction ($\mathrm{ms^{-1}}$)
v	Velocity component in y direction ($\mathrm{ms^{-1}}$)
W	Channel width of heat transfer fluid
x, y	Cartesian coordinates (m)

Greek symbols

β	Volumetric thermal expansion coefficient ($\mathrm{K^{-1}}$)
ΔT_{me}	Melting temperature window (K)
ε	Numerical constant
$\eta(T)$	Numerical step function
λ	Thermal conductivity ($\mathrm{Wm^{-1}K^{-1}}$)
μ	Dynamic viscosity ($\mathrm{Nsm^{-2}}$)
ρ	Density ($\mathrm{kgm^{-3}}$)

Subscripts

c	Copper
HTF	Heat transfer fluid
$lNePCM$	Liquid nano-enhanced phase change material
$sNePCM$	Solid nano-enhanced phase change material
me	Melting point

Abbreviations

$GNPs$	Graphite nanoplates
$LHTES$	Latent heat thermal energy storage
MVF	Melted volume fraction
$NePCM$	Nano-enhanced phase change material
PCM	Phase change material
PVT	Photovoltaic thermal
Ra	Rayleigh number

References

1. Chen, F.; Huang, R.; Wang, C.; Yu, X.; Liu, H.; Wu, Q.; Qian, K.; Bhagat, R. Air and PCM cooling for battery thermal management considering battery cycle life. *Appl. Therm. Eng.* **2020**, *173*, 115154. [CrossRef]
2. Elfeky, K.E.; Ahmed, N.; Wang, Q. Numerical comparison between single PCM and multi-stage PCM based high temperature thermal energy storage for CSP tower plants. *Appl. Therm. Eng.* **2018**, *139*, 609–622. [CrossRef]
3. Prieto, C.; Cabeza, L.F. Thermal energy storage (TES) with phase change materials (PCM) in solar power plants (CSP). Concept and plant performance. *Appl. Energy* **2019**, *254*, 113646. [CrossRef]
4. Teamah, H.M. Comprehensive review of the application of phase change materials in residential heating applications. *Alex. Eng. J.* **2021**, *60*, 3829–3843. [CrossRef]
5. Kong, X.; Wang, L.; Li, H.; Yuan, G.; Yao, C. Experimental study on a novel hybrid system of active composite PCM wall and solar thermal system for clean heating supply in winter. *Sol. Energy* **2020**, *195*, 259–270. [CrossRef]
6. Ling, Y.-Z.; Zhang, X.-S.; Wang, F.; She, X.-H. Performance study of phase change materials coupled with three-dimensional oscillating heat pipes with different structures for electronic cooling. *Renew. Energy* **2020**, *154*, 636–649. [CrossRef]
7. Abueluor, A.A.A.; Amin, M.T.; Abuelnour, M.A.; Younis, O. A comprehensive review of solar dryers incorporated with phase change materials for enhanced drying efficiency. *J. Energy Storage* **2023**, *72*, 108425. [CrossRef]
8. Al-Waeli, A.H.A.; Sopian, K.; Kazem, H.A.; Chaichan, M.T. Evaluation of the electrical performance of a photovoltaic thermal system using nano-enhanced paraffin and nanofluids. *Case Stud. Therm. Eng.* **2020**, *21*, 100678. [CrossRef]

9.   Mahdavi, M.; Tiari, S.; Pawar, V. A numerical study on the combined effect of dispersed nanoparticles and embedded heat pipes on melting and solidification of a shell and tube latent heat thermal energy storage system. *J. Energy Storage* **2020**, *27*, 101086. [CrossRef]

10.   Aqib, M.; Hussain, A.; Ali, H.M.; Naseer, A.; Jamil, F. Experimental case studies of the effect of Al_2O_3 and MWCNTs nanoparticles on heating and cooling of PCM. *Case Stud. Therm. Eng.* **2020**, *22*, 100753. [CrossRef]

11.   Eanest Jebasingh, B.; Valan Arasu, A. A comprehensive review on latent heat and thermal conductivity of nanoparticle dispersed phase change material for low-temperature applications. *Energy Storage Mater.* **2020**, *24*, 52–74. [CrossRef]

12.   Arshad, A.; Jabbal, M.; Sardari, P.T.; Bashir, M.A.; Faraji, H.; Yan, Y. Transient simulation of finned heat sinks embedded with PCM for electronics cooling. *Therm. Sci. Eng. Prog.* **2020**, *18*, 100520. [CrossRef]

13.   Ali, H.M.; Ashraf, M.J.; Giovannelli, A.; Irfan, M.; Irshad, T.B.; Hamid, H.M.; Hassan, F.; Arshad, A. Thermal management of electronics: An experimental analysis of triangular, rectangular and circular pin-fin heat sinks for various PCMs. *Int. J. Heat Mass Transf.* **2018**, *123*, 272–284. [CrossRef]

14.   Tiari, S.; Mahdavi, M.; Qiu, S. Experimental study of a latent heat thermal energy storage system assisted by a heat pipe network. *Energy Convers. Manag.* **2017**, *153*, 362–373. [CrossRef]

15.   Mahdavi, M.; Tiari, S.; De Schampheleire, S.; Qiu, S. Experimental study of the thermal characteristics of a heat pipe. *Exp. Therm. Fluid Sci.* **2018**, *93*, 292–304. [CrossRef]

16.   Baby, R.; Balaji, C. Experimental investigations on thermal performance enhancement and effect of orientation on porous matrix filled PCM based heat sink. *Int. Commun. Heat Mass Transf.* **2013**, *46*, 27–30. [CrossRef]

17.   Xu, Y.; Ren, Q.; Zheng, Z.-J.; He, Y.-L. Evaluation and optimization of melting performance for a latent heat thermal energy storage unit partially filled with porous media. *Appl. Energy* **2017**, *193*, 84–95. [CrossRef]

18.   Motahar, S.; Alemrajabi, A.A.; Khodabandeh, R. Experimental study on solidification process of a phase change material containing TiO_2 nanoparticles for thermal energy storage. *Energy Convers. Manag.* **2017**, *138*, 162–170. [CrossRef]

19.   Kant, K.; Shukla, A.; Sharma, A.; Henry Biwole, P. Heat transfer study of phase change materials with graphene nano particle for thermal energy storage. *Sol. Energy* **2017**, *146*, 453–463. [CrossRef]

20.   Bondareva, N.S.; Sheremet, M.A. Conjugate heat transfer in the PCM-based heat storage system with finned copper profile: Application in electronics cooling. *Int. J. Heat Mass Transf.* **2018**, *124*, 1275–1284. [CrossRef]

21.   Essa, M.A.; Rofaiel, I.Y.; Ahmed, M.A. Experimental and Theoretical Analysis for the Performance of Evacuated Tube Collector Integrated with Helical Finned Heat Pipes using PCM Energy Storage. *Energy* **2020**, *206*, 118166. [CrossRef]

22.   Al-Jethelah, M.; Ebadi, S.; Venkateshwar, K.; Tasnim, S.H.; Mahmud, S.; Dutta, A. Charging nanoparticle enhanced bio-based PCM in open cell metallic foams: An experimental investigation. *Appl. Therm. Eng.* **2019**, *148*, 1029–1042. [CrossRef]

23.   Choi, S.-K.; Kim, S.-O.; Lee, T.-H.; Dohee, H. Computation of the Natural Convection of Nanofluid in a Square Cavity with Homogeneous and Nonhomogeneous Models. *Numer. Heat Transf. Part A Appl.* **2014**, *65*, 287–301. [CrossRef]

24.   Ebrahimi, A.; Dadvand, A. Simulation of melting of a nano-enhanced phase change material (NePCM) in a square cavity with two heat source–sink pairs. *Alex. Eng. J.* **2015**, *54*, 1003–1017. [CrossRef]

25.   Ayoubi Ayoubloo, K.; Bazgirkhoob, H.; Asareh, M.; Noghrehabadi, A.; Moosavi, R. Magnetic force impact on melting behavior of dilatant non-Newtonian phase change materials using a numerical approach. *Alex. Eng. J.* **2023**, *66*, 505–522. [CrossRef]

26.   Liu, G.; Xiao, T.; Wang, X.; Yang, X.; Li, H. Numerical analysis of inner heating tube position for improving solid-phase transition in a shell-and-tube heat accumulator. *Alex. Eng. J.* **2023**, *65*, 771–784. [CrossRef]

27.   Zhu, Z.-Q.; Liu, M.-J.; Hu, N.; Huang, Y.-K.; Fan, L.-W.; Yu, Z.-T.; Ge, J. Inward Solidification Heat Transfer of Nano-Enhanced Phase Change Materials in a Spherical Capsule: An Experimental Study. *J. Heat Transf.* **2017**, *140*, 022301. [CrossRef]

28.   Ren, Q.; Chan, C.L. GPU accelerated numerical study of PCM melting process in an enclosure with internal fins using lattice Boltzmann method. *Int. J. Heat Mass Transf.* **2016**, *100*, 522–535. [CrossRef]

29.   *COMSOL Multiphysics*®; v. 5.6; COMSOL AB: Stockholm, Sweden, 2020. Available online: https://www.comsol.com (accessed on 30 June 2023).

30.   Söderlind, G.; Wang, L. Adaptive time-stepping and computational stability. *J. Comput. Appl. Math.* **2006**, *185*, 225–243. [CrossRef]

31.   Kamkari, B.; Amlashi, H.J. Numerical simulation and experimental verification of constrained melting of phase change material in inclined rectangular enclosures. *Int. Commun. Heat Mass Transf.* **2017**, *88*, 211–219. [CrossRef]

32.   Hashem Zadeh, S.M.; Ghodrat, M.; Ayoubi Ayoubloo, K.; Sedaghatizadeh, N.; Taylor, R.A. Partial charging/discharging of bio-based latent heat energy storage enhanced with metal foam sheets. *Int. Commun. Heat Mass Transf.* **2022**, *130*, 105757. [CrossRef]